Size-Invariant Detection of Cell Nuclei in Microscopy Images

Sundaresh Ram*, *Member, IEEE*, and Jeffrey J. Rodríguez, *Senior Member, IEEE*

Abstract—**Accurate detection of individual cell nuclei in microscopy images is an essential and fundamental task for many biological studies. In particular, multivariate fluorescence microscopy is used to observe different aspects of cells in cultures. Manual detection of individual cell nuclei by visual inspection is time consuming, and prone to induce subjective bias. This makes automatic detection of cell nuclei essential for large-scale, objective studies of cell cultures. Blur, clutter, bleed-through, imaging noise and touching and partially overlapping nuclei with varying sizes and shapes make automated detection of individual cell nuclei a challenging task using image analysis. In this paper we propose a new automated method for fast and robust detection of individual cell nuclei based on their radial symmetric nature in fluorescence *in-situ* hybridization (FISH) images obtained via confocal microscopy. The main contributions are two-fold. 1) This work presents a more accurate cell nucleus detection system using the fast radial symmetry transform (FRST). 2) The proposed cell nucleus detection system is robust against most occlusions and variations in size and moderate shape deformations. We evaluate the performance of the proposed algorithm using precision/recall rates, F_β-score and root-mean-squared distance (RMSD) and show that our algorithm provides improved detection accuracy compared to existing algorithms.**

Index Terms—**Cell nucleus detection, FISH images, FRST, histogram thresholding.**

I. INTRODUCTION

THE detection of cells in fluorescent microscopy images is an important first task for many biological studies, including high throughput analysis of gene expression level, morphology, and quantifying molecular markers and phenotypes. Counting cells or knowing the concentration of specific cells such as red blood cells, viruses and pathogens in medicine can reveal important information about the progress of an infectious disease. Studies that examine the growth rate of microorganisms also require cell counting. Also cell migrations and deformations play an essential role in biological processes, such as parasite invasion, immune response, embryonic development, and cancer detection. Thus, there is a significant interest in these applications to be able to detect the individual cell nuclei with high accuracy.

Manual cell counting by visual inspection of these cells is difficult, labor intensive, time consuming, and a fatiguing process. This is due to various reasons such as fluctuating intensities and

morphological variations of the cells within images [1], variances in illumination [2], crowding and overlapping of cells of varying sizes and shapes, accidental and non-specific staining, low signal-to-noise ratio (SNR) [3], spectral unmixing errors, microscopy imaging limitations and the large number of cells that the pathologist has to count per image. Moreover, the task of manually counting cells can be subjective, differing from person to person, and even one time to another, leading to erroneous results. These factors serve as a motivation for designing an automated algorithm for the detection of cell nuclei. However, due to the reasons mentioned above, design of an automated algorithm for cell detection is challenging.

The cell detection tools within the commonly available microscopy software are usually based on traditional techniques such as correlation matching [4], [5], thresholding [6], morphological operations [7], and energy minimization and optimization [3]. These techniques suffer considerably due to over-generalization, limiting their use to very simple images collected/captured in a carefully constrained environment. Cell detection using correlation matching, for instance, does not perform well when the cell population exhibits a variety of sizes and shapes, or when the SNR is poor. Detection based on global thresholding fails for images that present strong intensity gradients and/or noise. Preprocessing with smoothing filters and adaptive thresholding helps but could lead to further merging of cells or nuclei. Application of watershed transforms for cell detection prevents such merging but often leads to over-segmentation. Detection of cells using morphological operations such as distance transforms or H-minima transforms are very dependent on the cell structure and shape and perform poorly in densely populated and overlapping cell regions. Energy minimization and optimization techniques minimize the internal energy within cells to detect the cells, but may lead to false detections for highly textured and overlapping cells. To overcome these limitations, existing software tools allow user-friendly interfaces to correct the results obtained. This, however, results in losing the benefits of automation such as speed and reproducibility.

Recently, several new methods have been proposed for automated detection of cell nuclei for various applications [2], [3], [7]–[31]. Al-Kofahi *et al*. [3] proposed a cell detection algorithm using multiscale Laplacian-of-Gaussian (LoG) filtering constrained by distance-map-based adaptive scale selection. This method requires that the image histogram be bimodal and, for large and highly textured cells often causes undesirable splitting of nuclei. Dufour *et al*. [13] developed a cell detection scheme based on active surfaces, coupled by a penalty for overlaps. This method does not perform well when the cells are highly textured, and a wrong initialization of the active surface can lead to errors in detection. Dzyubachyk *et al*. [14]

proposed several improvements to Dufour's algorithm such as the use of the Radon transform to decouple the active surfaces of touching cells, thereby achieving detection of individual cell nuclei. Kong *et al.* [17] proposed a cell detection method using radial symmetry voting and concavity analysis. Using these two methods, the clustered cells are always partitioned via a line, which may not be the actual boundary separating them. Cheng *et al.* [7] apply active contour algorithm to separate the cells from background before using an adaptive H-minima transform to detect the individual cells. The cells are required to have a smooth intensity gradient profile for this method to perform well. Parvin *et al.* [22] introduced the iterative voting method, which uses oriented kernels for inferring saliency of the objects in order to detect them. This method produces a set of false seeds in the overlapping cell regions, when the intensity of the overlapping cell regions is brighter (or darker) than the non-overlapping regions within individual cells. Qi *et al.* [23] reported a cell detection algorithm involving fast, reliable object center localization approach that utilizes single-path voting followed by mean-shift clustering. This method performs well when we have a uniform cell size within an image, but detects false seeds when the cells are varying in size and shape.

In this paper we present a new automated technique for detection of cell nuclei in FISH images obtained via confocal microscopy, applied to the study of ovarian germline nurse cells of *Drosophila melanogaster* flies. We use the multiscale variance stabilizing transform (MS-VST) proposed by Zhang *et al.* [32] as a preprocessing step to reduce the noise in the images. We then binarize the images using a histogram thresholding technique to obtain a mask representing the cell nuclei in the image, which may touch each other in areas where they are densely populated. Next, we use the fast radial symmetric transform (FRST) to create a response image. Finally, we perform a dilation-based non-maximum suppression (NMS) on the generated response image to obtain a single seed/marker for each nucleus within the image. The key contributions of this paper are as follows:

- We present a computationally efficient cell nucleus detection algorithm in this work that exploits the radial symmetry nature of the cells using the FRST transform and provides accurate cell detection.
- Unlike other cell detection methods, this work describes a size-invariant cell nucleus detection scheme achieved using the automatic radius selection process in the FRST transform using the distance transform values from the binarized images.
- The algorithm is novel in the sense that it can efficiently handle detection of highly textured cells, a scenario where the prior developed methods tend to fail.

Precision/recall rates [3], [8], F_β-score [24], [33] and a pixel-wise distance error metric [34], [23] are used to measure the performance of the proposed nucleus detection algorithm.

II. MATERIALS

A. Labeling of Fish Probes and Hybridization

Conventional FISH protocols are cumbersome and time consuming. Below, we briefly describe the FISH protocol procedure as in [35], which was primarily adapted from [36].

About 1–2 day old female flies were flattened on yeast with male flies at 25°C for 2 days. Five ovary pairs were dissected in Grace's medium (Invitrogen) and fixed within 15 minutes. Fixation was performed for 4 minutes in 100 mM sodium cacodylate, 100 mM sucrose, 40 mM sodium acetate, 10 mM EGTA with 3.7% formaldehyde. Ovaries were washed twice for 5 minutes each in 2X SSCT (saline-sodium citrate, 0.2% Tween), and individual ovarioles were separated in 2X SSCT. Ovarioles were washed for 10 minutes each in 2X SSCT with 20%, 40%, and 50% formamide at room temperature and once more for 2 hours in 2X SSCT with 50% formamide at 37°C. About 200 – 500 ng of probe was mixed into a total of 40 mL hybridization buffer, denatured at 95°C, and snap frozen in liquid nitrogen. The formamide mixture was aspirated from ovarioles and replaced with a probe/hybridization buffer mixture. This suspension was mixed gently and incubated at 37°C for 10 minutes prior to a 2 minute denaturation at 92°C. Tubes were immediately returned to a hybridization oven and left overnight at the specified temperature. The next day, ovarioles were washed 4 times for 30 minutes each in 2X SSCT with 50% formamide at the hybridization temperature. Ovarioles were then washed 10 minutes each in 2X SSCT with 40% and 20% formamide. Three 5 minute washes with 2X SSCT were performed to remove the remaining formamide. The ovaries were stained with 10 ng/mL 4', 6-diamidino-2-phenylindole (DAPI) in 2X SSCT for 10 minutes and then washed twice with 2X SSCT for 10 minutes each. Ovarioles were mounted in VECTASHIELD. Pieces of number $1\frac{1}{2}$ coverslips were used as spacers between the actual coverslip and slide to prevent flattening of the egg chambers.

B. Image Acquisition

A Zeiss LSM 510 Meta confocal microscope (Carl Zeiss, Inc.) is used to acquire the images. A LP 420 DAPI filter at a wavelength of 405 nm was used to obtain the stained nucleus regions. Images were acquired with a Plan-Neofluar lens with magnification of $40 \times$, numerical aperture = 1.3, and a pixel size of 0.31 μm in the x and y-direction and 1 μm in the z-direction with automatic focusing. The signals emitted at specific wavelengths were absorbed by a photomultiplier tube and transformed into an intensity image according to the absorbed light. We followed a procedure similar to the one described in [35] and adjusted the gain and offset of the photomultiplier tubes in order to prevent the signals from getting over-saturated or under-saturated.

III. METHODS

The ovarian germline of the *Drosophila melanogaster* consists of two types of cells, namely "nurse cells" and "follicle cells" [37]. The follicle cells are smaller than the nurse cells and surround the nurse cells in an ellipsoidal fashion in 3-D. Both the follicle cells and nurse cells are brighter than the background region. Fig. 1(a) shows a single slice of a 3-D data set where the nurse cells are surrounded by smaller follicle cells lying along an elliptical ring. We define the background between the nurse cells and follicle cells as the inner background and the background between the follicle cells and the borders of the image as the outer background.
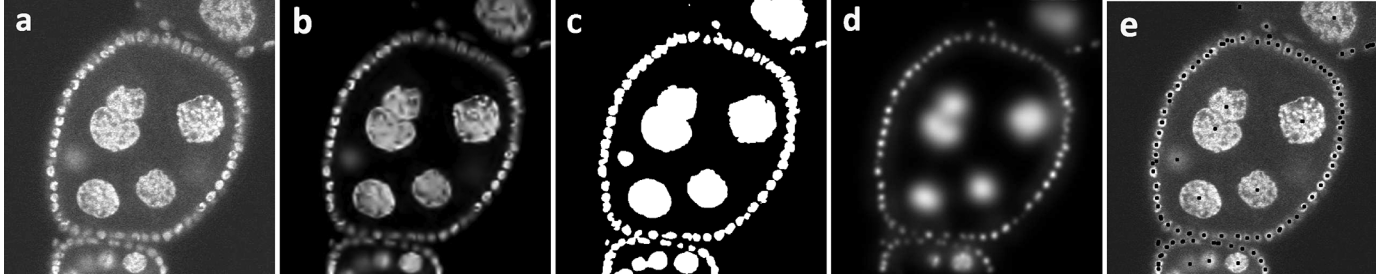
Fig. 1. Various steps of the proposed algorithm. (a) Original image. (b) Denoised image. (c) Image after thresholding and hole filling. (d) Image after applying FRST. (e) Detected seeds superimposed (indicated by black dots) onto original image after NMS.

A. Denoising

We use Zhang's denoising method (MS-VST) [32], which is particularly suited for denoising confocal microscope images as a preprocessing step to suppress the background noise significantly, thereby enhancing the image, making the separation between foreground and background modes better pronounced. The images obtained using the confocal microscope are corrupted by photon and camera readout noises and the stochastic data model is thus a mixed Poisson-Gaussian process (MPG). The MS-VST method models the dataset of discrete-space images as a d-dimensional MPG process $\mathbf{I} = (I_n)_{n \in \mathbb{Z}^d}$, where d is the number of image pixels and n contains the pixel coordinates. Thus, an observed image I_n is given by

$$I_n = \alpha X_n + Y_n, \ X_n \sim \mathcal{P}(\lambda_n), \ Y_n \sim \mathcal{N}(\mu, \sigma^2) \quad (1)$$

where $\alpha > 0$ is the overall gain of the detector, X_n is the Poisson variable of intensity λ_n modeling the photon counting, including the photon noise, Y_n is a normal variable representing readout noise, and both X_n and Y_n are assumed mutually independent. Image denoising aims at estimating the underlying intensity profile $\Lambda = (\lambda_n)_{n \in \mathbb{Z}^d}$ from $\mathbf{X}$, the random process representing the photon counts for the dataset. For image denoising, the MS-VST method incorporates a variance stabilizing transform (VST) into the filter banks of the isotropic undecimated wavelet transform (IUWT) [38], such that the noise-contaminated wavelet coefficients are asymptotically normally distributed with known constant variances. The VST operator T_j applied to each scale j is given by

$$T_j(a_j) = b^{(j)} \mathrm{sgn}(a_j + c^{(j)}) \sqrt{a_j + c^{(j)}} \quad (2)$$

where a_j are the wavelet approximation coefficients at each scale j ($\leq J$), $b^{(j)}$ is a constant related to $h^{(j)}$, the low-pass filter of the filter bank, and $c^{(j)}$ is a constant set according to [39]. Wavelet denoising is then achieved by zeroing the insignificant coefficients while preserving the significant ones under the control of false discovery rate (FDR) [40], which is the average fraction of false detections (i.e., zeroing the significant coefficients) over the total number of detections. After zeroing the insignificant coefficients, the MS-VST can be inverted in the same manner as the IUWT [38], but doing so could entail a loss of important structure from the images, due to the non-linear VST operator T_j. For this reason, MS-VST is inverted using a sparsity-driven iterative reconstruction technique as described in [39]. For the choice of the low-pass filter h in the IUWT, we

use a 2D separable B_3-spline filter as it is the most stable [41]. The unknown parameters α, μ, and σ are estimated by matching the first four cumulants of the image with the κ-statistics [42] of the samples as described in [41], in a uniform image region.

To find a uniform region within an image background, we compute the derivative of the low-pass filtered histogram of the original image, which has a L-shaped curve towards the larger gray-level bins of the histogram, and choose the gray-level bin corresponding to the maximum derivative magnitude as the threshold value. The pixels in the original image with gray level smaller than this threshold are selected as the samples to estimate the unknown parameters α, μ, and σ for the image. An example image before and after denoising is shown in Fig. 1(a) and (b), respectively. This preprocessing step works well for our images, but it may require minor modification for applications where the foreground and background gray levels have a very different relationship.

B. Binarization

The MS-VST denoising enhances the separation between modes in the bimodal histogram of the images as shown in Fig. 2. For our image data, the first peak of the histogram in Fig. 2 typically corresponds to the outer background, and the second peak consists of pixels belonging to the inner background and the foreground nuclei regions. We observe a deep valley between the two peaks and employ Otsu's thresholding [43] to remove the peak corresponding to the outer background from the histogram. The residual histogram is unimodal for our image data, with a steep monotonic increase till the peak is reached, followed by a Gaussian-like decay. It consists of two regions, the inner background region with the dominant peak and the foreground region present within the Gaussian-like decay part of the histogram. We use Rosin's method [44] to find a threshold to separate these two regions within the image. A straight line is drawn from the most populated point on the smoothed histogram curve to the first empty bin of the histogram following the final occupied bin. A line perpendicular to the first line is drawn from every point along the histogram curve between the most populated bin and the final occupied bin. The bin that has the maximum perpendicular distance to the first straight line is chosen as the threshold, which forms an initial binarization.

C. Refinements to Binarization

Since we have highly textured nuclei, we find that there are a few regions within the nucleus as well as near the border of
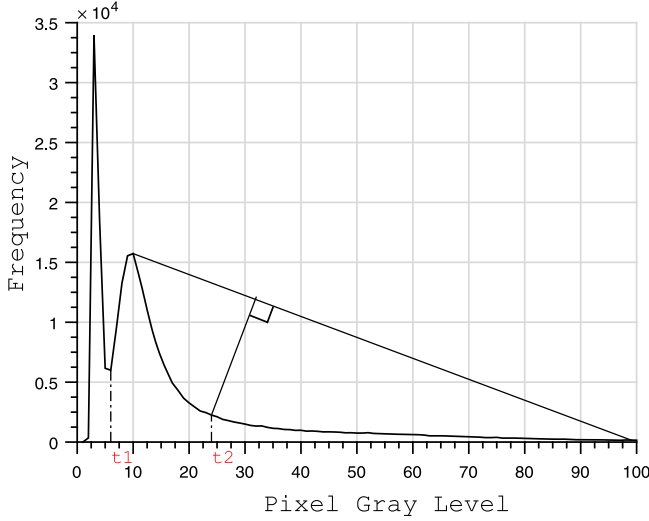
Fig. 2. Histogram of the denoised image. Otsu's method gives us threshold t1 as shown on the graph. The histogram to the right of threshold t1 is presented to Rosin's method, which gives us threshold t2 as indicated on the graph.
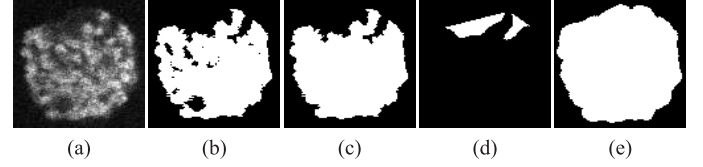

Fig. 3. Steps of the hole filling algorithm. (a) a representative single cell nucleus; (b) image after initial binarization; (c) image after filling all the holes within the cell nucleus; (d) missing foreground nucleus regions towards the border of the nucleus; (e) image after filling the borders of the cell nucleus.

the nucleus that are dark and are hence detected as background as shown in Fig. 3(b). Thus, we make additional refinements to the initial (Fig. 3(b)) binarization. First, we fill all the holes (dark regions within each nucleus in the initial binarization) using the application of morphological reconstruction. Let $\mathcal{I}$ denote the initial binarized image. We construct a new image $\mathcal{F}$ to be zero everywhere except on the one-pixel-wide image border, where it is set to $1 - \mathcal{I}$. Then we carry out dilation-based morphological reconstruction [45], using the complement of the initial binarized image $\mathcal{I}^c$ as the *mask* and the image $\mathcal{F}$ as the *marker* image, and using a 3×3 square structuring element. Finally, taking the complement of the morphologically reconstructed image leads to a binary image $\mathcal{I}$ with all the holes filled. Fig. 3(c) shows the result of filling all the holes within the nucleus. Next, in order to account for those foreground areas near the border of the nucleus that are detected as background (the missing "peripheral regions"), we dilate each nucleus region in the binarized image using a disk-shaped structuring element whose radius is computed automatically using the procedure described as follows. Our assumption is that cells have round/elliptical (i.e., convex) shapes. Thus, we expect to have a smoothly varying curvature along the cell boundaries. This is not entirely true, as the image obtained after binarization is often characterized by irregular and undulated contours as seen in Fig. 3(c). Therefore, in order to reduce those irregularities, we use wavelet shape descriptors to smooth out the boundaries of each cell nucleus, resulting in a smoothed binarized image [46]. Wavelet descriptors provide a powerful mathematical framework to reduce the irregularities of shape boundaries by eliminating the higher-order frequencies, which are representative of those irregularities. We then compute the convex hull of each nucleus in this smoothed binarized image and subtract it from the same image. The difference image approximately represents the peripheral regions that were missing in the initial binarization (refer to Fig. 3(d)). Parts of the boundaries of the peripheral regions originate from the chords formed by the

convex hull computation, and the other parts of the boundaries are the smoothed curves due to the wavelet shape descriptors. For each peripheral region, we calculate the maximum perpendicular distance between the chord part of the peripheral region and the smoothed curve part of the peripheral region denoted as d_n^t, where $n = 1, 2, 3, \ldots$ refer to the missing peripheral regions of a single nucleus and $t = 1, 2, 3, \ldots$ refer to the different nuclei within the whole image. Finally the radius of the disk-shaped structuring element for each nucleus is chosen as $r_t = \max_n \{d_n^t\}$. Fig. 3(e) shows the result after the refinements made to the binarized image of a single cell nucleus and Fig. 1(c) shows the result after refinement has been performed for a complete 2D image.

D. Fast Radial Symmetric Transform

Thresholding the denoised images and filling holes results in finding the regions in the image where the foreground nuclei are present. Thresholding helps to discriminate the individual foreground nuclei in areas where they are sparsely populated, but in areas where they are densely populated the nuclei appear connected to each other and we still need to discriminate the individual nuclei in these regions. We recognize that the shape of the nucleus plays an important role and helps our own eyes in detecting them individually, so we use the FRST method proposed by Loy *et al.* [47] to detect the individual nuclei in the densely populated areas. The FRST transform was originally developed to highlight points of interest in radially symmetric objects. It has been used for detection of rotational symmetries for various applications including iris detection [48], pupil localization [49], traffic sign detection [50], cell detection [31] and object matching.

The FRST is a computationally efficient, non-iterative procedure that computes the centers of radial symmetry along varying radii $\rho_{\min} \leq \rho \leq \rho_{\max}$ by operating along the direction of the image gradient. Since nuclei are somewhat radially symmetric objects, this operation is well suited for their localization. To produce the candidate nucleus locations, first the gradient $g(x)$ is calculated at each pixel x. For each integer radius ρ, an *orientation projection image* O_ρ and a *magnitude projection image* M_ρ are formed. These images are generated by examining the gradient g at a point x, from which a *positively affected pixel* $P_+(x)$ and a *negatively affected pixel* $P_-(x)$ are determined. The *positively affected pixel* is that pixel which the gradient $g(x)$ is pointing to, at a distance ρ from the location x, and the *negatively affected pixel* is that pixel which the gradient $g(x)$ is pointing away from, at a distance ρ from the location x. The

coordinates of $P_+(x)$ and $P_-(x)$ are given by the following equations.

$$P_+(x) = x + \text{Round}\left(\frac{g(x)}{\|\, g(x)\, \|}\rho\right) \qquad (3)$$

$$P_-(x) = x - \text{Round}\left(\frac{g(x)}{\|\, g(x)\, \|}\rho\right). \qquad (4)$$

The orientation and magnitude projection images are initially zero. For each pair $(P_+(x), P_-(x))$ of affected pixels, the corresponding pixel $P_+(x)$ in the image O_n and in the image M_n is incremented by 1 and $\|\, g(x)\, \|$, respectively, while the corresponding pixel $P_-(x)$ is decremented by the same quantities. The radial symmetry contribution at radius ρ is defined as a convolution,

$$S_\rho = F_\rho * G_\rho, \qquad (5)$$

where

$$F_\rho(x) = \frac{M_\rho(x)}{k_\rho}\left(\frac{|\, \tilde{O}_\rho(x)\, |}{k_\rho}\right)^\gamma$$

$$\tilde{O}_\rho(x) = \begin{cases} O_\rho(x) & \text{if } |\, O_\rho(x)\, | < k_\rho \\ k_\rho & \text{otherwise} \end{cases}. \qquad (6)$$

G_ρ is a two-dimensional Gaussian, γ is the radial strictness parameter, and k_ρ is a scaling factor that varies with ρ for normalizing M_ρ and O_ρ across different radii.

The FRST transform is defined as the average of the symmetry contributions over all radii considered,

$$S = \frac{1}{|\, N\, |}\sum_{\rho \in N} S_\rho \qquad (7)$$

where N is the set of radii being considered. In order to increase the computational speed of the algorithm, we compute the transform only at the *positively affected pixels* $P_+(x)$ and ignore the computation at *negatively affected pixels* $P_-(x)$ when we determine O_ρ and M_ρ, as our interest lies in the foreground nuclei regions, which appear brighter than the background. Also, we use a fixed G_ρ for all the radii. We apply this transform to the original image masked by the binarization obtained from Section III-B. This yields an output response image. Fig. 1(d) shows the resultant response image generated after applying the FRST.

E. Dilation-Based Non-Maximum Suppression

Since our image data consists of highly textured cell nuclei, the response image generated by carrying out the FRST transform may sometimes contain multiple small peaks located very close to the true large peak (to be detected) within the nurse cells (large cells). Also, in the densely populated regions where the nuclei appear clustered, the generated response image may at times contain erroneous small peaks in addition to the true peaks of the clustered nuclei, roughly equidistant from each of them. In order to overcome the two difficulties presented above and to obtain exactly one seed/marker per nucleus, we perform the following procedure: 1) grayscale dilation on the response image using a flat structuring element of size δ and 2) NMS of the dilated image.

The grayscale dilation of $A(x, y)$ by a flat structuring element $B(x, y)$ that has zero height everywhere is defined as

$$(A \oplus B)(x, y) = \max\{A(x - x', y - y')|(x', y') \in D_B\} \qquad (8)$$

where D_B is the domain of the structuring element B and $A(x, y)$ is assumed to be $-\infty$ outside the domain of the image. From (8) we can say that a grayscale dilation using a flat structuring element is a local-maximum operator. Thus, performing such a grayscale dilation with a structuring element of size δ gets rid of the small and erroneous peaks present within the response image. We then apply the NMS on the dilated image. NMS is the task of finding all the local maxima in an image. We follow the approach developed by Förstner and Gülch [51], where the image pixels are visited in a spiral scan order. Each visited pixel is compared to other pixels in its neighborhood and the central pixel is a non-maximum if a larger or equal neighbor is found [52]. Following such a procedure, we usually obtain exactly one seed per nucleus. Fig. 1(e) shows the detected seeds using the grayscale dilation and NMS overlaid (indicted by black dots) on the original image.

IV. PERFORMANCE EVALUATION METRICS

In order to evaluate the cell detection performance of each automated method we first run the connected component labeling algorithm [53] and obtain the set of labels $L(i, j)$ for all pixels, where $L(i, j) \in \{0, \ldots, K\}$, with $L = 0$ corresponding to the background and $L \neq 0$ denoting one of the K detected objects in the image. The centroid, x_k, is calculated for each of the K objects. The "ground truth" centroid x_G is obtained from the manually segmented nuclei in the real images. If the position of x_k lies within the boundary of the manually segmented nuclei, it is counted as a true positive (TP); otherwise it is considered a false positive (FP). In the case of multiple centroids detected within a manually segmented nucleus, the centroid x_k located closest to x_G of the manually segmented nucleus is selected as a TP and the rest are considered FPs. The number of false negatives (FN) is defined as $N_G - N_{\text{TP}}$, where N_G is the number of objects in the ground truth and N_{TP} is the number of TPs. A true negative (TN) is defined as accurate detection of a region not to be an object. Since we count the background as a single object that is not a nucleus, the number of TNs in our problem is undefined. We consider four common measures to evaluate the performance of the algorithms.

A. FROC Curve

The FROC curves [54] were generated for each automated method by collecting the pairs of the true positive ratio (TPR) and the false positives per image (FPR*) for different thresholds. We compute these two quantities as:

$$\text{TPR} = \frac{N_{\text{TP}}}{N_{\text{TP}} + N_{\text{FN}}} = \frac{N_{\text{TP}}}{N_G}, \quad \text{FPR}^* = \frac{N_{\text{FP}}}{N_G}. \qquad (9)$$

For the proposed method, the FRST transformed image is normalized within the range [0, 255]. The points on the FROC curve for the proposed method are generated by thresholding the normalized FRST transformed image using values between

0 and 255, while fixing all the other parameters of the algorithm. For Al-Kofahi's MS-LoG method, we obtain the FROC curve by varying the standard deviation value σ of the Gaussian filter, while fixing all other parameters. For Parvin's IRV-K method, we generate the FROC curve by varying the "vote image" threshold, while fixing all the other parameters. For Qi's SPV-MS method, we obtain the FROC curve by varying the bandwidth of the mean shift filter, while fixing all other parameters.

B. Coverage Measure

The coverage measure, also known as F_{β}-score or F-measure [24], [29], is a measure of a test's detection accuracy in statistics. It considers both precision $\mathcal{P}$ and recall $\mathcal{R}$ of the test to compute the score. It is defined as

$$F_{\beta} = (1 + \beta^2) \cdot \frac{\mathcal{P} \cdot \mathcal{R}}{(\beta^2 \cdot \mathcal{P}) + \mathcal{R}} \qquad (10)$$

where the precision $\mathcal{P}$ and recall $\mathcal{R}$ are defined by

$$\mathcal{P} = \frac{N_{\mathrm{TP}}}{N_{\mathrm{TP}} + N_{\mathrm{FP}}}, \quad \mathcal{R} = \frac{N_{\mathrm{TP}}}{N_{\mathrm{TP}} + N_{\mathrm{FN}}}. \qquad (11)$$

In this paper we use F_1 (i.e., $\beta = 1$) as this is the most common choice for this type of evaluation.

C. Tanimoto Coefficient

The Tanimoto coefficient (TC) [55], also known as Tanimoto distance, is a statistic used for comparing the similarity and diversity of two sample sets. It is defined as

$$\mathcal{T} = \frac{N_{\mathrm{TP}}}{M + N_G - N_{\mathrm{TP}}} \qquad (12)$$

where M is the number of detected objects in any automated detection algorithm, N_G is the number of objects in the ground truth and N_{TP} is the number of TPs.

D. Root-Mean-Squared Distance

We compute the root-mean-squared distance (RMSD) as a measure of localization accuracy of the various automated detection algorithms. Let us denote the set $A = \{a_i, i = 1, \ldots, N_{\mathrm{TP}}\}$ as the locations of all the detected TPs in an image using an automated detection algorithm, and the set $G = \{g_i, i = 1, \ldots, N_G\}$ as the set of corresponding true object locations in the ground truth image with $N_{\mathrm{TP}} \leq N_G$. Then we can define RMSD as

$$d(A, G) = \left\{ \frac{1}{N_{\mathrm{TP}}} \sum_{i=1}^{N_{\mathrm{TP}}} \{a_i - g_i\}^2 \right\}^{1/2}. \qquad (13)$$

V. Experiments and Results

The proposed method for individual cell nucleus detection has been applied to both synthetic and real data across various application domains. We compare our algorithm with three other state-of-the-art cell nucleus detection algorithms: Al-Kofahi's distance-constrained multiscale Laplacian-of-Gaussian detector (MS-LoG) [3], Parvin's iterative radial voting scheme using oriented kernels (IRV-K) [22], and Qi's detector based on single-pass voting and mean-shift segmentation (SPV-MS)

[23]. We show that our algorithm is tolerant to varying size and geometry of nuclei, has excellent noise immunity, and can effectively detect overlapping cell nuclei with varying intensities.

A. Algorithm Parameter Settings

In the FRST transform, the radius is varied over the range

$$1 \leq \rho \leq 2 \times \max \{D(x, y)\} \qquad (14)$$

where $D(x, y)$ is the distance transform of the binarized image. The variance of the Gaussian kernel is $\sigma_{\rho}^2 = (1/2)\rho$ for each $\rho \in [\rho_{\min}, \rho_{\max}]$. The optimal values for the radial strictness parameter γ and scaling factor k_{ρ} in FRST and the structuring element size δ for grayscale dilation are automatically selected using the alternate free-response receiver operating characteristics (AFROC) curves [54] by varying one parameter at a time while keeping the others fixed and choosing that value of the parameter which maximizes the area under the curve (AUC).

B. Synthetic Data

We generated synthetic images with additive white Gaussian noise at various signal-to-noise ratio (SNR) levels. Fig. 4 shows the detection of individual cell nuclei by several automated cell detection algorithms on the synthetic image with overlapping nuclei with varying intensities when the signal-to-noise ratio (SNR) is varied from 10 dB to -10 dB. The detection results are marked by white dots for 10 dB and 5 dB SNR images and by black dots for -5 dB and -10 dB SNR images. From Fig. 4 we observe that the proposed method is able to detect all the 11 circular objects individually without any false detections until an SNR of -5 dB, whereas other methods under comparison have either missed detection or have false detections even at SNRs 10 dB and 5 dB. At a SNR of -10 dB all of these methods produces false detections, but the proposed method also detects each circular object exactly once, unlike the other methods which have either multiple detections per circular object or missed detections. In addition to demonstrating the sensitivity to noise, we also demonstrate the proposed method's sensitivity to scaling. In Fig. 5 we consider three circular objects with various radii and overlap values along each row: 5 & 80%, 15 & 60%, 25 & 40%, and 35 & 20%. From the detection results shown in Fig. 5, we observe that the proposed method is able to detect the three overlapping circular objects very well regardless of the percentage of overlap between them, whereas the other methods detect either less or more than three objects as the scale (radius) varies. These results indicate the tolerance of the proposed method to noise and scale for a well-defined object.

C. FISH Image Data

The proposed method was mainly developed with the goal to detect cell nuclei in the germline of *Drosophila Melanogaster*. For many biological studies, it is important to detect and segment these cells so as to identify the physical location of sub-cellular structures such as genes and the organization of chromatin within each nucleus. In our experiments, the x- and y-dimensions of each image acquired are 504×512 pixels. We collected an image data set of 260 images (Data Set 1) consisting of a total of 4302 cells (915 nurse cells and 3387 follicle cells). A careful
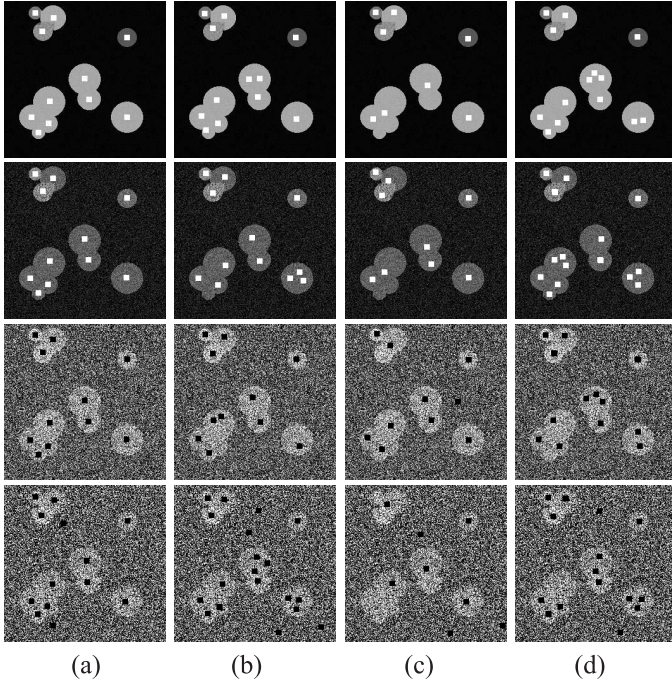
Fig. 4. Detection of cells for a synthetic image containing overlapping circular cells of varying intensities for various SNR levels. Columns 1–4 show detection using proposed method, SPV-MS, MS-LoG, and IRV-K, respectively. Rows 1–4 have cell SNR of 10 dB, 5 dB, -5 dB, and -10 dB, respectively. (a) Proposed. (b) SPV-MS. (c) MS-LoG. (d) IRV-K.
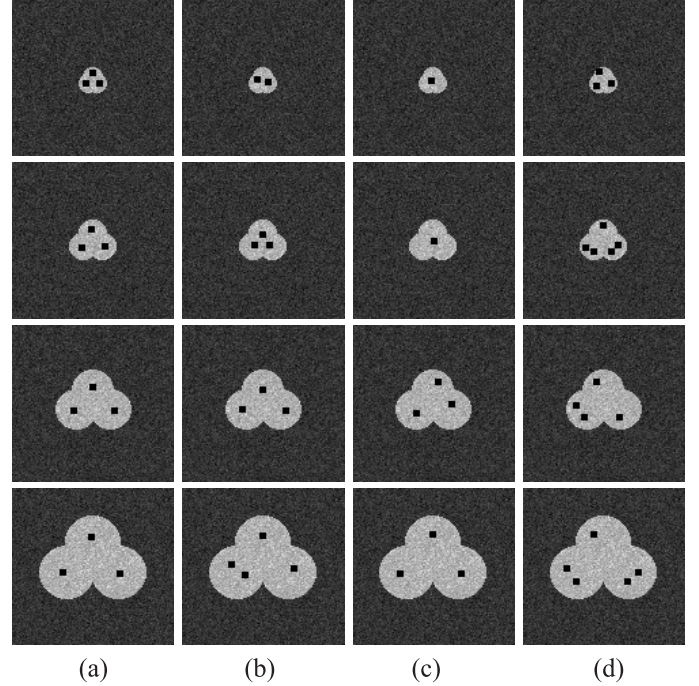

Fig. 5. Detection of cells for synthetic images containing three overlapping circular cells. Columns 1–4 show results using proposed method, SPV-MS, MS-LoG, and IRV-K, respectively. Rows 1–4 have cell radii (in pixels) and overlap values of 5 & 80%, 15 & 60%, 25 & 40%, and 35 & 20%, respectively. (a) Proposed. (b) SPV-MS. (c) MS-LoG. (d) IRV-K.

manual segmentation of every cell in the 260 images was performed and the centroids of each segmented cell in these images were considered as ground truth detections for all subsequent analysis. The parameter values of our method were automatically chosen using the AFROC AUC analysis described in Section V-A. The radial strictness parameter in FRST was chosen to be $\gamma = 2$, the scaling factor in FRST was chosen to be $k_\rho = 10$ and the structuring element for grayscale dilation was chosen as $\delta = 7$. For a fair comparison between the proposed automated method and the other automated techniques under comparison, the parameters of the other automated techniques were automatically chosen using the AFROC AUC analysis for the FISH image datasets. For the MS-LoG method the minimum scale for the LoG filter was chosen as $\sigma_{\min} \in [3, 9]$, and the maximum scale for the LoG filter was chosen as $\sigma_{\max} \in [12, 38]$. For the IRV-K algorithm the minimum radial range was $\sigma_{\min} = 1$, the maximum radial range was $\sigma_{\max} = 20$, the angular range was $\Delta_N = 25$, the scale for computing image gradient was $\Gamma_g = 3$, and the voting threshold $\Gamma_v = 500$. For the SPV-MS method the estimated average diameter of the cell was $d = 26$, and the angular range was $\Delta = 34$.

The qualitative detection results for two example images from our data set of 260 images are shown in Fig. 6. From Fig. 6(a) we notice that the proposed method is able to detect exactly one seed for all the small cells packed very close together at the top-right corner of the image. The detection results for all the other automated methods shown in Fig. 6(b)–(d) indicate that these methods fail to detect all the cells in the top-right corner of the image where the cells appear very densely populated and close to each other. For the large cells

towards the center of the image, which are highly textured due to the chromatin structure, our proposed method in Fig. 6(a) detects each cell nucleus exactly once as compared to the other automated methods in Fig. 6(b)–(d), which get confused and yield multiple detections for each cell nucleus in the image. Also from Fig. 6(e) we observe that the proposed method is able to detect exactly one seed per cell for cells around the center region of the image, where the boundary information is incomplete (perceptual boundary grouping), whereas the results of the other methods shown in Fig. 6(f)–(h) indicate multiple seeds detected per cell.

The quantitative performance of the automated methods is presented in Table I. The first half of Table I shows the results using the 260 FISH images referenced as Data Set 1. Table I shows that the F_1-score of the proposed method is 6.2 percentage points greater than Qi's SPV-MS method, 9.3 percentage points greater than Al-Kofahi's MS-LoG method, and 4.3 percentage points greater than Parvin's IRV-K method. Fig. 7 shows the FROC curves. Fig. 7 shows that the proposed method has better detection accuracy compared to the other automated methods at all points along the curve. Table I also shows that the proposed method has the best TC among all the evaluated methods. In terms of localization accuracy, we observe from Table I that the mean RMSD for the proposed method is 2.1 pixels smaller than Qi's SPV-MS method, 2.9 pixels smaller than Al-Kofahi's MS-LoG method, and 2.2 pixels smaller than Parvin's IRV-K method. This shows that the proposed method localizes the cells better than the other methods.

We also compared the proposed algorithm to the other methods in terms of speed. We ran all the algorithms on a total
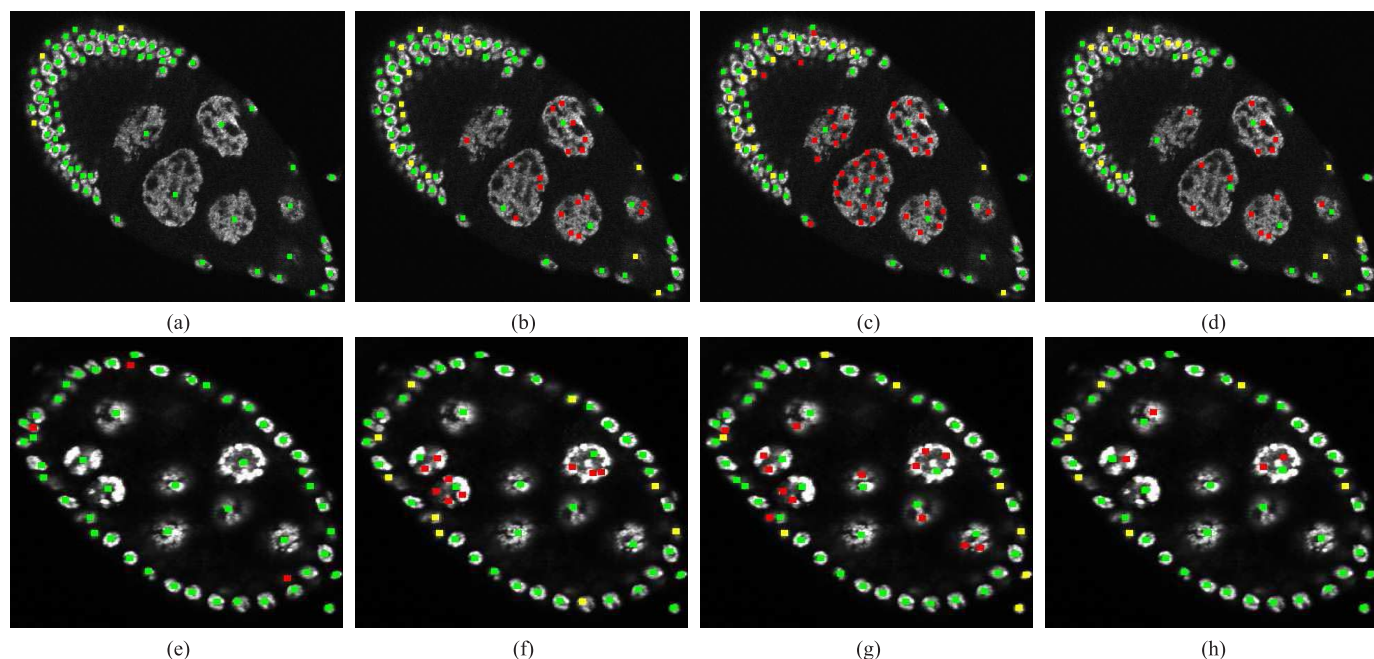
Fig. 6.   Detection of individual cells for two example images from the FISH image dataset using: Column 1: proposed method, Column 2: SPV-MS, Column 3: MS-Log, and Column4: IRV-K. True positives, false positives and false negatives are represented by green, red, and yellow dots, respectively in the color version of this paper.

TABLE I
MEAN PERFORMANCE (AND STANDARD DEVIATION) FOR VARIOUS ALGORITHMS

Methods	Precision ($\mathcal{P}$)		Recall ($\mathcal{R}$)		F_β-score		Tanimoto Coefficient ($\mathcal{T}$)		RMSD (d)	
Data Set 1 (DS1)										
Proposed Method	**0.881**	**(0.011)**	**0.809**	**(0.015)**	**0.846**	**(0.012)**	**0.854**	**(0.029)**	**6.016**	**(0.821)**
SPV-MS Method	0.808	(0.021)	0.762	(0.013)	0.784	(0.017)	0.756	(0.069)	8.102	(1.373)
MS-LoG Method	0.769	(0.031)	0.738	(0.019)	0.753	(0.024)	0.735	(0.052)	8.921	(1.192)
IRV-K Method	0.813	(0.016)	0.794	(0.011)	0.803	(0.014)	0.783	(0.045)	8.249	(1.453)
Data Set 2 (DS2)										
Proposed Method	**0.962**	**(0.023)**	**0.925**	**(0.042)**	**0.943**	**(0.030)**	**0.934**	**(0.024)**	**3.723**	**(0.728)**
SPV-MS Method	0.912	(0.042)	0.899	(0.028)	0.910	(0.034)	0.886	(0.022)	5.732	(0.907)
MS-LoG Method	0.940	(0.051)	0.897	(0.032)	0.918	(0.040)	0.910	(0.031)	4.725	(0.842)
IRV-K Method	0.922	(0.047)	0.901	(0.025)	0.911	(0.033)	0.879	(0.023)	4.814	(0.865)
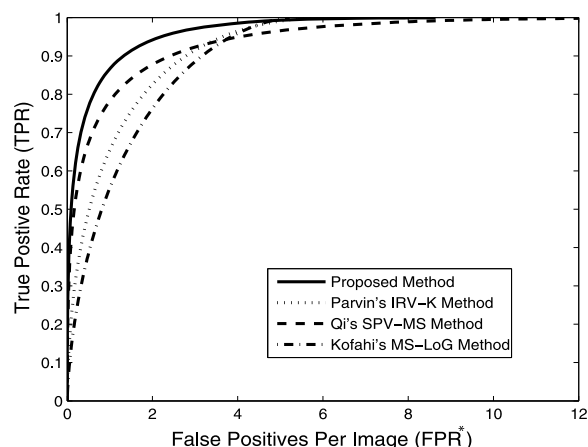
Fig. 7.   FROC curves for all the automatic detection methods.

TABLE II
MEAN COMPUTATION TIME (AND STANDARD DEVIATION)
FOR VARIOUS ALGORITHMS IN SECONDS

Methods	Computation Time
Proposed Method	**3.917 (1.273)**
SPV-MS Method	7.915 (1.873)
MS-LoG Method	11.841 (2.023)
IRV-K Method	8.163 (1.722)

of 100 microscopy images from Data Set 1, each consisting of many nuclei. Table II shows the mean and standard deviation of running time each method takes to detect the nuclei. The proposed method and Qi's SPV-MS method were coded using MATLAB. For Al-Kofahi's MS-LoG method and Parvin's IRV-K method, we obtained the source code online[1]. The whole process was carried out on a 2.1 GHz, 3 GB RAM, Intel Dual

[1]The obtained source code for Al-Kofahi's MS-LoG method is in MATLAB, whereas source code for Parvin's IRV-K method obtained online is coded using Java. We used the MIJ package at http://bigwww.epfl.ch/sage/soft/mij to run the IRV-K code using the MATLAB environment.
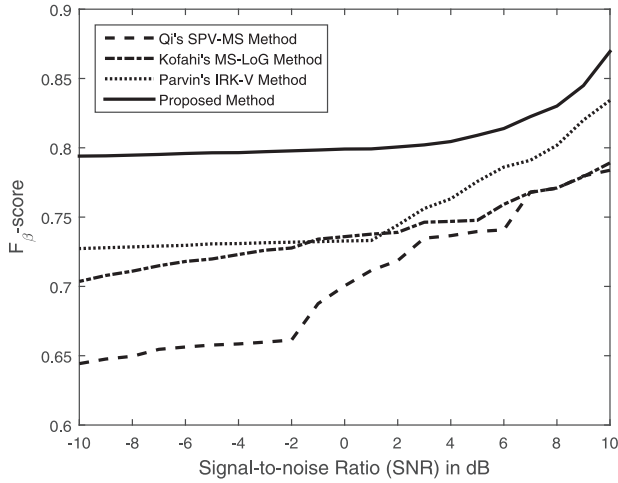
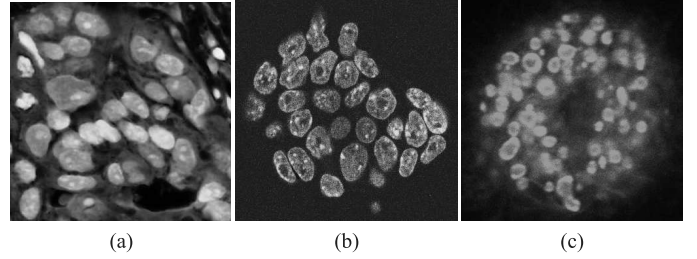Fig. 8. Mean F_1-score of all automated methods at various SNR levels.

Fig. 9. Several microscopy images of cell nuclei at various physical scales. (a) Histopathology image of skin cancer tissue, which is stained to highlight squamous cells (331×346); (b) PCNA-GFP-labeled CHO cell image (331×341); (c) Epi-fluorescence microscopy HeLa cell image (366×366).

Core, Windows PC. Table II shows that the proposed method runs 3.9 seconds faster than Qi's SPV-MS method, 7.9 seconds faster than Al-Kofahi's MS-LoG method, and 4.2 seconds faster than Parvin's IRV-K method. Qi's SPV-MS method involves the calculation of votes for every pixel having large gradient magnitude followed by mean shift clustering and thus takes more time to execute. Al-Kofahi's MS-LoG method takes more time to execute because of the multiscale LoG filtering step needed to create the response image. Parvin's IRV-K method uses an iterative voting scheme for each object within the image, where voting is performed in an angular range and thus takes more time to execute.

Finally, we compared the algorithms with respect to noise robustness. We added white Gaussian noise at various SNR levels to a representative subset of 50 images from Data Set 1, and ran all the algorithms on each of these noisy images. Fig. 8 shows the mean F_1-score for each algorithm as the SNR is varied between -10 dB and 10 dB. Fig. 8 shows that the detection accuracy of the proposed method is better than the other methods at all SNR levels.

D. Online Data

To further show the robustness of the proposed algorithm, we used image set BBBC004v1[2] (herein referred to as Data Set 2) from the publicly available Broad Bioimage Benchmark Collection (BBBC) [56]. The BBBC004v1 image set consists of 100 synthetic images simulated with 300 cells per image, organized into five groups of 20 images each. Each image is partitioned into six equally sized regions. The simulated cells are placed within each image either using a uniform distribution or assigned to one of the six regions within each image in the five groups with probabilities of 0% & 100%, 15% & 85%, 30% & 70%, 45% & 55%, and 60% & 40%, respectively. The second half of Table I shows the detection performance of the algorithms using Data Set 2. From Table I we observe that the F_1-score of the proposed method is 3.3 percentage points greater than Qi's SPV-MS method, 2.5 percentage points greater than Al-Kofahi's MS-LoG method, and 3.2 percentage points

[2]www.broadinstitute.org/bbbc/index.html

greater than Parvin's IRV-K method. Table I also shows that the proposed method performs better than the other methods in terms of TC. In addition to detection accuracy, the proposed method is better in terms of localization accuracy in comparison to the other methods as it has the smallest RMSD value in Table I.

E. Other Application Data

Cell nucleus detection for several example cell images from different modes of microscopy at different physical scales will now be demonstrated. The first group of example cells, shown in Fig. 9(a), shows highly differentiated squamous cells of the mouth from a histopathology image of skin cancer tissue. This type of skin cancer tends to arise from pre-malignant lesions, and it is thus very important to detect and identify the individual cell nuclei for early detection of the cancer and appropriate treatment. The image shows cells with varying intensities, which are overlapping each other. The size of this image is 331×346, and cell radius in this image lies within the range $[20, 72]$ pixels. Fig. 10 shows the cell nucleus detection results of the automated methods. We notice from Fig. 10(a) that the proposed method is able to detect most of the cells individually without making any false detections. The results from Fig. 10(b)–(d) indicate the presence of multiple detections per cell in some areas of the image and false detections in areas of the image where there are no cells present.

The second group of example cells, shown in Fig. 9(b) corresponds to cell nucleus detection and tracking in time-lapse fluorescence microscopy, which is of importance in many biological studies on cell migration and proliferation rates. In this case, it is important to detect and track the individual cell nuclei to answer questions of how stem cells, progenitor cells, and various leukocyte subtypes migrate throughout the body, and how their states of differentiation and activation vary depending upon their location or interaction with each other and, in the case of immune cells, with antigen and antigen-presenting cells. The image shown in Fig. 9(b) is a 2D PCNA-GFP-labeled CHO cell image extracted from a 3D dataset using time-lapse fluorescence microscopy imaging. Due to specific PCNA-GFP staining, the image has a low SNR and shows textures having multiple areas of high intensity at irregular positions within each cell, with cells touching each other. The size of this image is 331×341 and cell radius in this image lies within the range $[7, 60]$ pixels. Fig. 11 shows the detection results for this image,
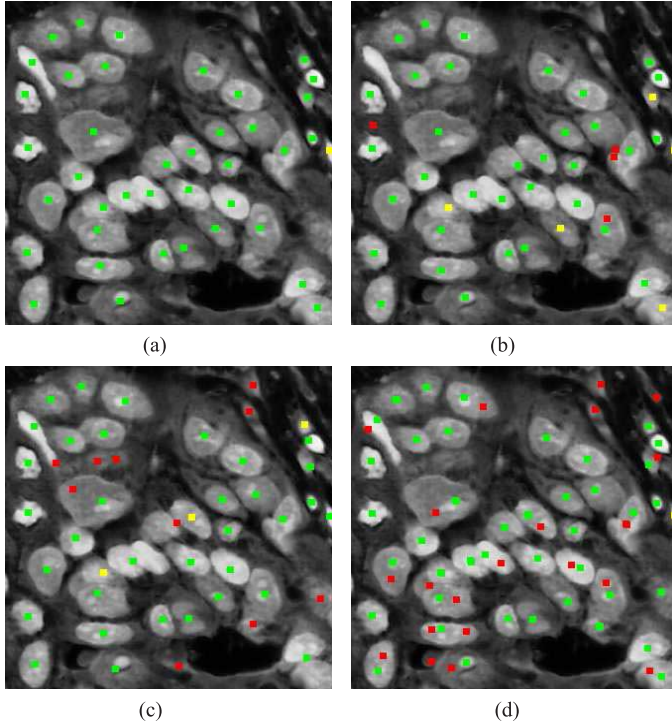
Fig. 10. Detection of individual cell nuclei in the histopathology skin cancer image from Fig. 9(a). This image consists of 40 cells. True positives (TP), false positives (FP) and false negatives (FN) are represented by green, red, and yellow dots, respectively in the color version of this paper.
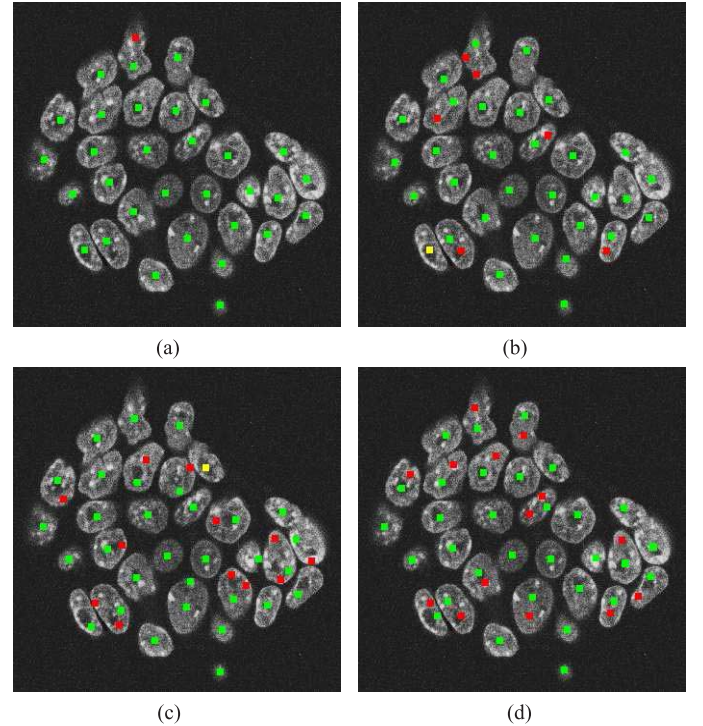

Fig. 11. Detection of individual cell nuclei in the PCNA-GFP-labeled CHO image from Fig. 9(b). This image consists of 31 cells. True positives (TP), false positives (FP) and false negatives (FN) are represented by green, red, and yellow dots, respectively in the color version of this paper.

using the various detection methods. The proposed method is able to detect each nucleus separately, whereas the other automated methods have errors in detection.

The third group of example cells, shown in Fig. 9(c) relates to a study of nuclear localization in developmental biology for the evaluation of many cellular functions including proliferation rates. In this case, the samples at different time points are fixed and imaged with an epi-fluorescence microscope to examine the kinetics of cell division in the human epithelial carcinoma cell line (HeLa) model system under different treatments. They are highly proliferative and undergo constant regeneration. They undergo mitosis, where the chromosomes in the nucleus are divided and separated into two identical sets, followed by the division of the cell into two identical daughter cells. It is thus important to detect or identify the number of cell nuclei that are present at any given time so as to track and quantify the division process. The epithelial HeLa cells shown in Fig. 9(c) are undergoing mitosis, so the cells have varying sizes and look blurred with the low contrast in comparison to the background. The size of this image is 366×366 and cell radius in this image lies within the range [4, 35] pixels. The detection results are shown in Fig. 12, where we observe that the proposed method is able to identify the cells with varying sizes whereas the other methods have detection errors.

VI. DISCUSSION AND CONCLUSION

Accurate detection of individual cell nuclei in microscopy images is a challenging task for a manual user, as well as for any automated cell detection algorithm. In this paper we propose a solution to this problem. Our method combines MS-VST
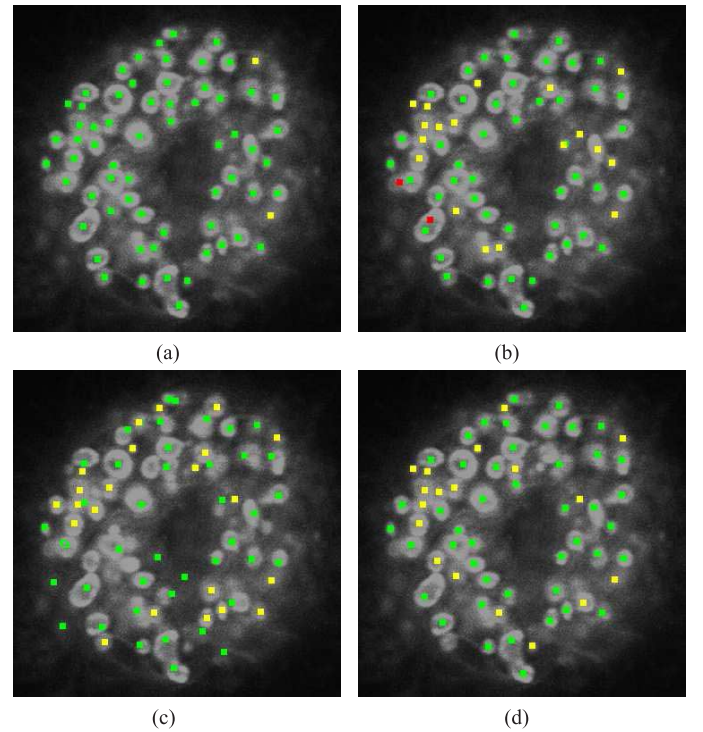

Fig. 12. Detection of individual cell nuclei in the epithelial HeLa cell image from Fig. 9(c). This image consists of 65 cells. True positives (TP), false positives (FP) and false negatives (FN) are represented by green, red, and yellow dots, respectively in the color version of this paper.

filtering to suppress noise, histogram-based thresholding to find the foreground regions, computation of FRST and use of a dilation-based NMS procedure to find and detect the individual
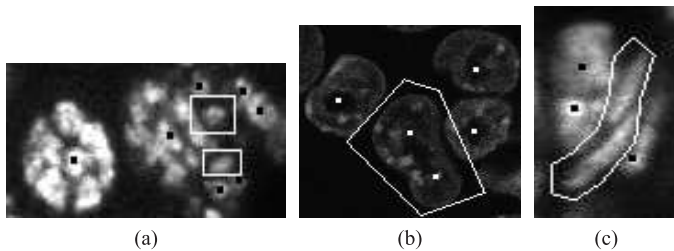
(a)　　　　　　　(b)　　　　　　　(c)

Fig. 13. Examples of detection errors produced by our algorithm.

cell nuclei. Parvin's IRV-K method [22] uses an iterative radial voting scheme with varying kernels, and Qi's SPV-MS method [23] uses a single-pass voting followed by mean-shift clustering to detect the cells. Both these methods assume an estimated average diameter for the cells and use a fixed radial range. Kofahi's MS-LoG method [3] takes a different approach by using a multi-scale LoG filtering constrained by an adaptive scale selection in order to detect the cells. Our approach differs from these earlier methods. We do not choose a fixed radial range or do an adaptive scale selection, as the key idea of the work presented in this paper is to be able to detect cells with varying sizes and high texture/fluctuating intensities within them. Applying the FRST transform in combination with the dilation-based NMS makes our method robust to detect cells of varying sizes and high textures within the images.

The algorithm was first validated with respect to detection accuracy using the FROC curve, coverage measure, and Tanimoto coefficient. Second, the algorithm was validated with respect to localization accuracy using the RMSD. Table I shows that the proposed method performs the best among all the methods compared for both datasets tested. Fig. 6 shows that the proposed method qualitatively performs the best in comparison to the other methods. To show that the proposed method is general and can be applied to various other types of cell images, we ran the algorithms on three other types of cell images shown in Fig. 9. The results for these images are shown in Figs. 10–12, which show that the proposed method is the best among all the methods compared.

Finally, we present some inherent limitations of the automated methods. Fig. 13 shows some example cases where all the algorithms including our algorithm fail to produce optimal detection results. In Fig. 13(a) we observe that the algorithm has missed two small cells (indicated by a square box around them) in the vicinity of a large cell by confusing them to be a part of the large cell due to the detailed texture present within the large cell. In Fig. 13(b) we see that the algorithm has wrongly identified a single cell as two different cells (indicated by a polygon around it) due to the dumbbell-like shape this cell presents. This could be due to the fact that the algorithm expects the cells to be round objects, thereby identifying two round objects inside the polygonal region in Fig. 13(b). Similarly, Fig. 13(c) shows that the algorithms have missed detection of two elongated cells (indicated by a polygon around them), again due to the shape they present.

REFERENCES

[1] S. Ram, J. J. Rodriguez, and G. Bosco, "Size-invariant cell nucleus segmentation in 3-D microscopy," in *Proc. IEEE Southwest Symp. Image Anal. Interpretation*, 2012, pp. 37–40.

[2] M. E. Plissiti, C. Nikou, and A. Charchant, "Automated detection of cell nuclei in Pap smear images using morphological reconstruction and clustering," *IEEE Trans. Inf. Technol. Biomed.*, vol. 15, no. 2, pp. 233–241, Mar. 2011.

[3] Y. Al-Kofahi, W. Lassoued, W. Lee, and B. Roysam, "Improved automatic detection and segmentation of cell nuclei in histopathology images," *IEEE Trans. Biomed. Eng.*, vol. 57, no. 4, pp. 841–852, Apr. 2010.

[4] F. Raimondo *et al.*, "Automated evaluation of Her-2/neu status in breast tissue from fluorescent in situ hybridization images," *IEEE Trans. Image Process.*, vol. 19, no. 4, pp. 1288–1299, Sep. 2005.

[5] C. Chen, W. Wang, J. A. Ozolek, and G. K. Rohde, "A flexible and robust approach for segmenting cell nuclei from 2D microscopy images using supervised learning and template matching," *Cytometry Part, A*, vol. 83A, no. 5, pp. 495–507, May 2013.

[6] N. Phansalkar, S. More, A. Sabale, and M. Joshi, "Adaptive local thresholding for detection of nuclei in diversity stained cytology images," in *Proc. Int. Conf. Commun. Signal Process.*, 2011, pp. 218–220.

[7] J. Cheng and C. Rajapakse, "Segmentation of clustered nuclei with shape markers and marking function," *IEEE Trans. Biomed. Eng.*, vol. 56, no. 3, pp. 741–748, Mar. 2009.

[8] C. Aeteta, V. Lempitsky, J. A. Noble, and A. Zisserman, "Learning to detect cells using non-overlapping extremal regions," in *Proc. MICCAI*, 2012, pp. 348–356.

[9] J. Byun *et al.*, "Automated tool for the detection of cell nuclei in digital microscopic images: Application to retinal images," *Molecular Vis.*, vol. 12, pp. 949–960, Aug. 2006.

[10] J. D. Vylder, J. Aelterman, M. Vandewoestyne, T. Lepez, D. Deforce, and W. Philips, *Cell Nuclei Detection using Globally Optimal Active Contours with Shape Prior*. Berlin, Germany: Springer, 2012, vol. 7432, LNCS, pp. 115–124.

[11] K. N. Chaudhury, Z. Puspoki, A. Munoz-Barrutia, D. Sage, and M. Unser, "Fast detection of cells using a continuously scalable Mexican-hat-like template," in *Proc. IEEE Int. Symp. Biomed. Imag.*, 2010, pp. 1277–1280.

[12] G. Cong and B. Parvin, "Model-based segmentation of nuclei," *Pattern Recognit.*, vol. 33, no. 8, pp. 1383–1393, Apr. 2000.

[13] A. Dufour *et al.*, "Segmenting and tracking fluorescent cells in dynamic 3-D microscopy with coupled active surfaces," *IEEE Trans. Image Process.*, vol. 14, no. 9, pp. 1396–1410, Sep. 2005.

[14] O. Dzyubachyk, W. A. van Cappellen, J. Essers, W. J. Niessen, and E. Meijering, "Advanced level-set-based cell tracking in time-lapse fluorescence microscopy," *IEEE Trans. Med. Imag.*, vol. 29, no. 3, pp. 852–867, Mar. 2010.

[15] C. Jung and C. Kim, "Segmenting clustered nuclei using H-minima transform-based marker extraction and contour parameterization," *IEEE Trans. Biomed. Eng.*, vol. 57, no. 10, pp. 2600–2604, Oct. 2010.

[16] C. Jung, C. Kim, S. W. Chae, and S. Oh, "Unsupervised segmentation of overlapped nuclei using Bayesian classification," *IEEE Trans. Biomed. Eng.*, vol. 57, no. 12, pp. 2825–2832, Dec. 2010.

[17] H. Kong, M. Gurcan, and K. Belkacem-Boussaid, "Partitioning histopathological images: An integrated framework for supervised color-texture segmentation and cell splitting," *IEEE Trans. Med. Imag.*, vol. 30, no. 9, pp. 1661–1677, Sep. 2011.

[18] C. F. Koyuncu, S. Arslan, I. Durmaz, R. C.- Atalay, and C. G.- Demir, "Smart markers for watershed-based cell segmentation," *PLoS ONE*, vol. 7, no. 11, p. e48664, Nov. 2012.

[19] A. Karsnas, A. L. Dahl, and R. Larsen, "Learning histopathological patterns," *J. Pathol. Inf.*, vol. S12, no. 2, Jan. 2011.

[20] G. Li *et al.*, "3D cell nuclei segmentation based on gradient flow tracking," *BMC Cell Biol.*, vol. 8, no. 40, Sep. 2007.

[21] N. Malpica *et al.*, "Applying watershed algorithms to the segmentation of clustered nuclei," *Cytometry*, vol. 28, no. 4, pp. 289–297, Aug. 1997.

[22] B. Parvin *et al.*, "Iterative voting for inference of structural saliency and characterization of subcellular events," *IEEE Trans. Image Process.*, vol. 16, no. 3, pp. 615–623, Mar. 2007.

[23] X. Qi, F. Xing, D. J. Foran, and L. Yang, "Robust segmentation of over-lapping cells in histopathology specimens using parallel seed detection and repulsive level set," *IEEE Trans. Biomed. Eng.*, vol. 59, no. 3, pp. 754–765, Mar. 2012.

[24] P. Quelhas, M. Marcuzzo, A. M. Mendonca, and A. Campilho, "Cell nuclei and cytoplasm joint segmentation using the sliding band filter," *IEEE Trans. Med. Imag.*, vol. 29, no. 8, pp. 1463–1473, Aug. 2010.

[25] A. Samborskiy, "Cell detection and counting for microscope images with applications to stem cell engineering," M.S. thesis, Dept. Elect. Comp. Eng., Carnegie Mellon Univ., Pittsburgh, PA, 2007.

[26] O. Schmitt and M. Hasse, "Radial symmetries based decomposition of cell clusters in binary and gray level images," *Pattern Recognit.*, vol. 41, no. 6, pp. 1905–1923, Jun. 2008.

[27] Q. Wen, H. Chang, and B. Parvin, "A Delaunay triangulation approach for segmenting clumps of nuclei," in *Proc. IEEE Int. Symp. Biomed. Imag.*, 2009, pp. 9–12.

[28] W. Xiong, S.-C. Chia, and J. H. Lim, "Automated nuclei decomposition for image analysis in neuronal cell fluorescent microscopy," in *Proc. IEEE Int. Conf. Image Process.*, 2011, pp. 1577–1580.

[29] P. Yan, X. Zhou, M. Shah, and S. T. C. Wong, "Automatic segmentation of high-throughput RNAI fluorescent cellular images," *IEEE Trans. Inf. Technol. Biomed.*, vol. 12, no. 1, pp. 109–117, Jan. 2008.

[30] L. Yang, O. Tuzel, P. Meer, and D. J. Foran, "Automatic image analysis of histopathology specimens using concave vertex graph," in *Proc. MICCAI*, 2008, pp. 833–841.

[31] N. Timilsina, C. Moffatt, and K. Okada, "Development of a stained cell nuclei counting system," in *Proc. SPIE Med. Imag., Image Process.*, 2011, vol. 7962, p. 79620k.

[32] B. Zhang, M. J. Fadili, J. L. Starck, and J. C. Olivo-Marin, "Multiscale variance-stabilizing transform for mixed-Poisson-Gaussian processes and its applications in bioimaging," in *Proc. IEEE Int. Conf. Image Process.*, 2007, pp. 233–236.

[33] I. Smal, M. Loog, W. Niessen, and E. Meijering, "Quantitative comparison of spot detection methods in fluorescence microscopy," *IEEE Trans. Med. Imag.*, vol. 29, no. 2, pp. 282–301, Feb. 2010.

[34] S. Ram and J. J. Rodriguez, "Symmetry-based detection of nuclei in microscopy images," in *Proc. IEEE Int. Conf. Acoust., Speech, Signal Process.*, 2013, pp. 1128–1132.

[35] S. Ram and J. J. Rodriguez, "Segmentation and detection of fluorescent 3D spots," *Cytometry Part A*, vol. 81A, no. 3, pp. 198–212, Jan. 2012.

[36] A. F. Derburg, *Drosophila Protocols*, W. Sullivan, M. Ashburner, and R. S. Hawley, Eds., 1st ed. New York, USA: Cold Spring Harbor, 2000, pp. 25–55.

[37] A. C. Spradling, *The Development of Drosophila Melanogaster*, M. Bate and A. M. Arias, Eds. New York: Cold Spring Harbor, 1993, pp. 1–70.

[38] J. L. Starck, M. J. Fadili, and F. Murtagh, "The undecimated wavelet decomposition and its reconstruction," *IEEE Trans. Image Process.*, vol. 16, no. 2, pp. 297–309, Feb. 2007.

[39] B. Zhang, M. J. Fadili, and J. L. Starck, "Wavelets, ridgelets, and curvelets for Poisson noise removal," *IEEE Trans. Image Process.*, vol. 17, no. 7, pp. 1093–1108, Jul. 2008.

[40] Y. Benjamini and D. Yekutieli, "The control of false discovery rate in multiple testing under dependency," *Ann. Stat.*, vol. 29, no. 4, pp. 1165–1188, Aug. 2001.

[41] B. Zhang, "Contributions to fluorescence microscopy in biological imaging: PSF modeling, image restoration, and super-resolution detection," Ph.D. dissertation, Dept. TSI, Ecole Superieure des Telecommun., Paris, France, 2007.

[42] C. Rose and M. D. Smith, *Mathematical Statistics with Mathematics*. Berlin, Germany: Springer-Verlag, 2002, pp. 256–259.

[43] N. Otsu, "A threshold selection method from gray-level histograms," *IEEE Trans. Syst., Man, Cybern.*, vol. 9, no. 1, pp. 62–66, Jan. 1979.

[44] P. Rosin, "Unimodal thresholding," *Pattern Recognit.*, vol. 34, no. 11, pp. 2083–2096, Nov. 2010.

[45] P. Soille, *Morphological Image Analysis: Principles and Applications*. New York: Springer-Verlag, 2003.

[46] G. C.-H. Chuang and C.-C. J. Kuo, "Wavelet descriptor of planar curves: Theory and applications," *IEEE Trans. Image Process.*, vol. 5, no. 1, pp. 56–70, Jan. 1996.

[47] G. Loy and A. Zelinsky, "Fast radial symmetry for detecting points of interest," *IEEE Trans. Pattern Anal. Mach. Intell.*, vol. 25, no. 8, pp. 959–973, Aug. 2003.

[48] D. W. Hansen and Q. Ji, "In the eye of the beholder: A survey of models for eyes and gaze," *IEEE Trans. Pattern Anal. Mach. Intell.*, vol. 32, no. 3, pp. 478–500, Mar. 2010.

[49] P. Yang, B. Du, S. Shan, and W. Gao, "A novel pupil localization method based on GaborEye model and radial symmetry operator," in *Proc. IEEE Int. Conf. Image Process.*, 2004, pp. 67–70.

[50] A. Mogelmose, M. M. Trivedi, and T. B. Moeslund, "Vision-based traffic sign detection and analysis for intelligent driver assistance systems: Perspective and survey," *IEEE Trans. Intell. Transp. Syst.*, vol. 13, no. 4, pp. 1484–1497, Dec. 2012.

[51] W. Förstner and E. Gülch, "A fast operator for detection and precise locations of distinct points, corners, and centers of circular features," in *Proc. Intercommision Conf. Fast Process. Photogrammetric Data*, 1987, pp. 281–305.

[52] T. Q. Pham, *Non-Maximum Suppression using Fewer than Two Comparisons per Pixel*. Berlin, Germany: Springer, 2010, vol. 6474, LNCS, pp. 438–451.

[53] R. M. Haralick and L. G. Shapiro, *Robot Vision*, 1st ed. Reading, MA: Addison-Wesley, 1992, vol. 1.

[54] D. P. Chakraborty and K. S. Berbaum, "Observer studies involving detection and localization: Modeling, analysis and validation," *Med. Phys.*, vol. 31, no. 8, pp. 2313–2330, Aug. 2004.

[55] R. O. Duda, P. E. Hart, and D. G. Stork, *Pattern Classification*, 2nd ed. Hoboken, NJ: Wiley, 2001.

[56] V. Ljosa, K. L. Sokolnicki, and A. E. Carpenter, "Annotated high-throughput microscopy image sets for validation," *Nature Methods*, vol. 9, no. 7, p. 637, Jul. 2012.